Prasanna, Malith; Wei, Mingdong; Polojärvi, Arttu; Cole, David M.

Laboratory experiments on floating saline ice block breakage in ice-to-ice contact

Published in:
Cold Regions Science and Technology

DOI:
10.1016/j.coldregions.2021.103315

Published: 01/09/2021

Cold Regions Science and Technology 189 (2021) 103315

Contents lists available at ScienceDirect

Cold Regions Science and Technology

journal homepage: www.elsevier.com/locate/coldregions

Laboratory experiments on floating saline ice block breakage in ice-to-ice contact

Malith Prasanna [a,*], Mingdong Wei [a], Arttu Polojärvi [a], David M. Cole [b]

[a] Aalto University, School of Engineering, Department of Mechanical Engineering, P.O. Box 14100, FI-00076 Aalto, Finland
[b] ERDC-CRREL (Ret.), 72 Lyme Rd., Hanover, NH 03768, USA

ARTICLE INFO

Keywords:
Saline ice
Breakage
Ice-to-ice contact
Force chain
Shear failure

ABSTRACT

This study uses a unique experimental system to explore the breakage of laboratory-grown, floating saline ice blocks under ice-to-ice contacts. This topic is important to the understanding and modeling of force transmission through ice rubble fields. In a collection of ice blocks subjected to compressive loading, force is transmitted via force chains, and their stability plays a crucial role in ice-structure interaction processes. Peak loads are limited by the buckling of these force chains or breakage at the ice block contacts. Lack of information on the breakage mechanism motivates the present effort. In the experiments, three ice blocks were set up to form two ice-to-ice contacts, after which the three-block system was compressed to failure. The force transmitted through each contact and the failure process of the blocks were recorded. In total 32 tests with varying contact areas were performed. In about 75% of the cases, the load transmitted by an ice-to-ice contact was limited by shear failure. The key property limiting the magnitude of the force transmitted by an ice-to-ice contact was found to be shear strength; blocks typically failed in shear on planes having the characteristics of 'Coulombic shear faults'. Quasi-static force equilibrium analysis of these shear failures showed that the floating ice blocks with a naturally occurring temperature gradient used in this study had a shear strength of 279 kPa. Other failure modes, including crushing, splitting and 'Y-shaped' conjugate failure, were occasionally observed.

1. Introduction

In cold regions, the complex interaction process between floating ice features and engineering structures causes ice loads on structures. When an ice sheet collides with a structure, it breaks into ice blocks, which can form an ice rubble pile. Interactions among the ice sheet, the rubble pile and the structure lead to a series of peak ice load events (Daley et al., 1998). Peak ice loads are due to series of ice blocks in contact with each other and the structure under high compressive stress. Such arrangements are called force chains (Peters et al., 2005), commonly known to transmit loads through granular media such as gravel, soil or ice rubble. To illustrate this phenomenon, Fig. 1 presents a snapshot from a simulation of interaction between a floating ice sheet and an inclined structure. The figure shows that compressive force is transmitted preferentially through a specific series of blocks (the force chain), and not generally through the rubble field. Magnitudes of the peak loads applied to the structure are limited by the failure of such force chains. The failure may occur due to the buckling of the force chain or local failure at the block-to-block contacts (Paavilainen and Tuhkuri, 2013; Ranta et al., 2018; Ranta and Polojärvi, 2019). Local failure at contacts were visually observed to occur in direct shear box experiments on ice rubble by Pustogvar et al. (2014), but this process has not been thoroughly studied, thus providing motivation for the present study.

An ice block subjected to compressive forces can break through various failure modes such as splitting, shearing, spalling or crushing (Schulson, 2001; Tuhkuri, 1994). The mode depends on the confinement of the ice block, specimen preparation methods controlling the parallelism and flatness of the faces, loading rate and direction of the forces relative to the grain direction of ice (Gagnon, 2018; Kuehn et al., 1993; Schulson, 2001; Schulson and Duval, 2009). In addition, the boundary conditions of the block influence the failure mode. Uniaxial compression experiments by Schulson et al. (1989) showed that the friction at the ice specimen-loading apparatus interface could change the failure mode of the specimen from axial splitting to shearing, and consequently, increases the force bearing capacity of the specimen. A similar effect of contact at loading platens in compressive strength experiments has been reported in other studies as well (Schulson and Duval, 2009). Thus, it is evident that the ice-to-ice contact condition has an influence on the

* Corresponding author.
E-mail address: malith.prasanna@aalto.fi (M. Prasanna).

https://doi.org/10.1016/j.coldregions.2021.103315
Received 2 October 2020; Received in revised form 19 May 2021; Accepted 25 May 2021
Available online 27 May 2021

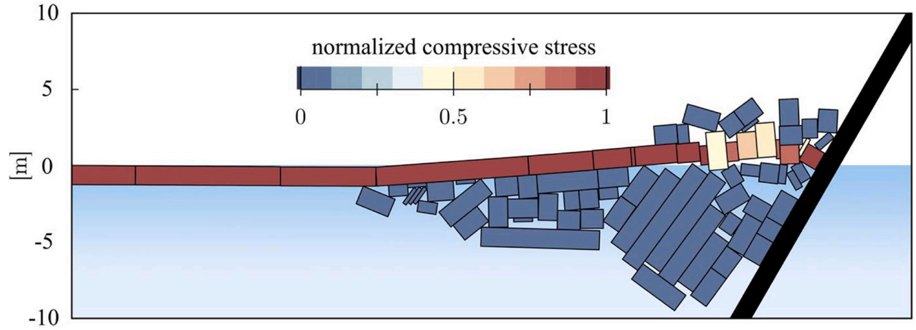

Fig. 1. A snapshot from an ice-structure interaction simulation showing a force chain (Ranta and Polojärvi, 2019). The simulation presented here is of a moving floating ice sheet colliding with an inclined structure. A force chain (ice block arrangement in contact due to high compressive stress) transmitting force from the intact ice sheet to the inclined structure can be noticed.

failure mode of blocks in a force chain. However, to our best knowledge, there has not been any previous experimental study on the breakage of ice blocks under ice-to-ice contact forces, although such studies related to other materials, such as rock and concrete, exist (Chang et al., 2018; Zhao et al., 2020).

Detailed understanding of the mechanics of breakage is important for numerical modeling purposes. Numerical modeling of ice blocks can employ either physically based or phenomenological approaches. In physically based modeling, failure is simulated using constitutive equations coupled with explicit failure criteria. Thus, failure force of the block, failure mode and size of the fragments are controlled by constraints within the numerical model. This type of numerical modeling of ice blocks has been performed using Extended Finite Element Method (Moore et al., 2013), Cohesive Surface Methodology (Kolari, 2017; Kuutti et al., 2013) and Bonded Particle Method (Ji et al., 2017, 2015). On the other hand, block breakage is simulated as a single event in phenomenological modeling. Once the stresses applied on the block have reached the defined failure criterion, the block is considered broken and replaced by its fragments. Generally, the failure criterion and fragment size distribution for these models are based on empirical data. Phenomenological breakage modeling methods, namely the fragment replacement method (Cleary, 2001; Delaney et al., 2015) are widely used in simulating comminution processes in rock mechanics but have never been applied to ice blocks. In Discrete Element Method simulations, it is common to use contact force laws that on some level account for ice block failure. Usually this is done by setting the upper limit of the contact pressure based on the compressive or crushing strength of ice (Hopkins, 1992; Paavilainen et al., 2009; Tuhkuri and Polojärvi, 2018; van den Berg et al., 2018). It is worth highlighting that block breakage in a rubble pile is a comminution process due to the interaction of many ice blocks; thus, physically based modeling of block breakage is not ideal in large scale simulations presented in Fig. 1 due to its high computational costs. Modeling of ice rubble as a continuum and using continuum breakage mechanics to model the block breakage is one way of addressing the computational cost (Kulyakhtin, 2019). Continuum breakage theories are widely used in geomechanics to model crushable granular materials under confined compressive stresses (Daouadji and Hicher, 2010; Einav, 2007). Continuum models, however, are not capable of capturing crucial features such as ice block accumulation and force chains within an ice rubble pile. Thus, while phenomenological modeling of block breakage is a promising technique for large scale ice rubble simulations, the physical experiments on the scale of individual ice blocks, as conducted in the work described below, are a prerequisite for the reliable use of such models.

The present work focuses on laboratory-scale experiments on breakage. Such experiments are often performed using relatively cold and dry ice samples, either grown in the laboratory or harvested from the sea. Most of the sea ice in nature is, however, relatively warm and floating and thus has a through-thickness temperature gradient with most of the ice being very close to its melting point. Moreover, brine drainage upon sample removal from the water will decrease the brine volume in the sample (Weeks and Hibler, 2010). As the mechanical behavior of ice depends on such ice properties as temperature, salinity, density, porosity, crystal type and crystal orientation (Timco and Weeks, 2010), the dry and cold ice specimens behave differently from most of the ice in nature (Cole and Dempsey, 2004; Wei et al., 2020). Thus, in situ experiments with floating ice specimens are an important method to study the mechanical behavior of natural ice. In the case of compressive

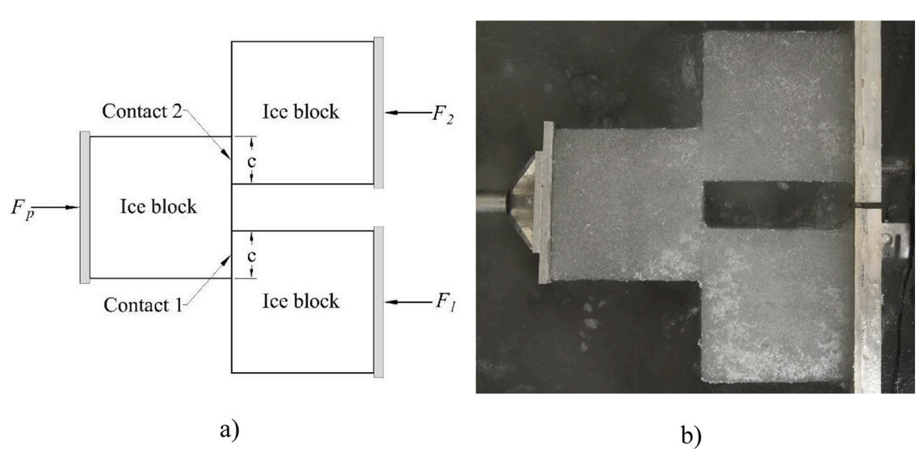

Fig. 2. Illustration of the three-block system studied: (a) illustration of the set-showing two contacts of length c, the piston force, F_p, and the reaction forces F_1 and F_2, and (b) photograph of the setup.

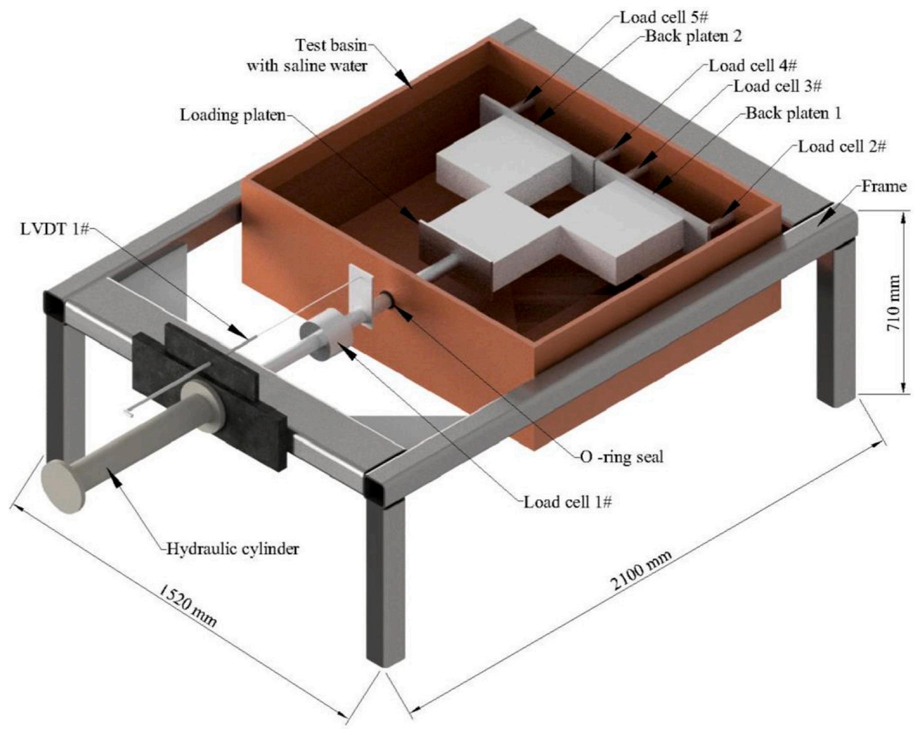

Fig. 3. Illustration of the testing rig. The three ice specimens had nominal dimensions of 300 mm × 300 mm × 110 mm. The test basin had inner dimensions of 1300 mm × 1100 mm × 400 mm.

failure of floating ice, however, there have been very few such studies (Timco and Weeks, 2010). Here we use a newly developed experimental set-up allowing laboratory-scale experiments on laboratory-grown saline, floating, ice blocks with a naturally occurring temperature gradient. The breakage experiments conducted here are the first of their kind. The objective of these experiments is to generate fundamental data on ice block breakage under ice-to-ice contact forces when the contact geometry is rather simple, but the contact size varies. Such data are important for understanding the limit mechanisms for ice loads and in developing numerical models for describing ice behavior; what limits the load that the ice blocks compressed together may transmit? Thus, the primary interest here was to measure the maximum force transmitted by the contact and to study the failure modes.

The paper is organized as follows. Section 2 describes the laboratory ice specimens used in the experiments, the experimental setup, the procedures related to breakage experiments and the test matrix. Section 3 presents the experimental results, including the force-time curves, the magnitudes of maximum contact forces and a detailed description of the failure process. The analysis and discussion related to the results are given in Section 4. The focus of this section is on the shear failure of the ice blocks and the difference between the failure of contact in an ice-to-ice contact and an ice-to-metal contact. Finally, Section 5 concludes the paper.

2. Experiments

Wei et al. (2020) described the ice growing tank, the ice growing procedure and the loading rig used in more detail. Briefly, the ice was grown and the experiments were performed in the cold room of Department of Mechanical Engineering, Aalto University. Fig. 2 illustrates the basic concept of the ice block breakage experiments, designed conservatively to mimic the type of contacts that could be expected to have the ability to transmit the highest loads within a force chain (Fig. 1). Three ice blocks were removed from the ice growing tank, set floating, brought into contact, and compressed until the failure of blocks. Compressive force applied by the hydraulic piston, F_p, and two reaction forces F_1 and F_2 were recorded. Forces F_1 and F_2, were the main interest, since they are equal to the forces transmitted by the two specimen-to-specimen contacts. Experiments were conducted for six contact length, c, values. The three-block configuration was chosen as it was symmetric and inhibited block rotation. Moreover, it allowed easy adjustments of the contact length without having to change the ice block dimensions or to make other adjustments on the experimental setup.

2.1. Ice specimen preparation and characterization

Breakage experiments were performed using laboratory-grown, saline ice specimens having nominal dimensions of 300 mm × 300 mm × 110 mm (width × length × thickness). Ice was grown in a tank with dimensions of 1150 mm × 1150 mm × 980 mm and was made from insulated plywood sheets. High-density polyethylene molds were used when growing the ice to control the dimensions of the specimens (Wei et al., 2020); dimensional accuracy of the specimen dimensions was ±2 mm. The specimens thus produced required no further preparation. Inconsistent block geometries could significantly influence failure modes of the specimens under compression (Schulson and Duval, 2009). In addition, special attention was given to the ice growing process in order to obtain ice sheets with reproducible properties. We generally obtained nine specimens from one ice sheet.

The ice was grown from saline water made by mixing tap water and "Red Sea: Coral Pro" aquarium salt. The water salinity was 24 ppt for all the ice sheets. The ice had a density of 886 kgm^{-3} and a melt-water salinity of 5 ppt. The ice growing process was initiated by seeding the water surface of the ice growing tank with fine mist of freshwater having a temperature of 0 °C. After seeding, the air temperature in the cold room was maintained at −14 °C for three days for fast ice growth and then at −10 °C for another two days to stabilize the temperature of the ice sheet; all experiments were carried out at −10 °C air temperature in the same cold room. Langway Jr (1958) described the techniques used to study the thin sections made from the ice to confirm that it had type S2 columnar microstructure with random c-axis orientation in the horizontal plane. The average grain size of the ice produced by the above method was approximately 3 mm.

Once the ice thickness had reached 110 mm, the ice blocks were ejected from the molds and immediately transferred to the testing rig. As explained in the next section, the testing rig consisted of a saline water basin where ice specimens were set to float. Since the rig was in the same cold room with the ice growing tank, the specimens could be moved from the growing tank into the test basin quickly with no significant temperature change or brine drainage. Typical time duration between the removal of the specimens from the growing tank and the end of their breakage experiment was 30 min. A three-channel temperature data logger (Extech SD200) was used to monitor the through-thickness temperature of the floating ice blocks in the test basin, as reported in Wei et al. (2020). The floating ice blocks had a relatively stable temperature profile for the duration of the experiments. Typical temperature readings were − 3.0 °C, −2.3 °C and − 2.2 °C for top, middle and bottom parts of the ice block, respectively; the average ice temperature was −2.5 °C.

2.2. Experimental setup and procedure

Breakage experiments were performed using a force-controlled uniaxial compression testing rig. Fig. 3 presents the ice specimens and the rig in a configuration used in the experiments. The rig consisted of a main frame constructed of square tube welded steel sections, a hydraulic cylinder, loading platen, two back-platens, test basin, five load cells and a displacement gauge. The hydraulic cylinder was rigidly mounted on the frame, had a loading capacity of 100 kN and was controlled by an electro-hydraulic servo valve (EHSV). The test basin was made of waterproof plywood sheets and had inner dimensions of 1300 mm × 1100 mm × 400 mm. It was partially filled with water from the ice growing tank, which ensured that the water temperature and salinity in the test basin and growing tank were the same. The piston of the hydraulic cylinder passed through a sealed port on the wall of the test basin. Frictional resistance of this port was negligible (Wei et al., 2020). Three specimens were set to float between the loading plate and two back-platens as per the configuration presented in Fig. 2.

As Fig. 3 illustrates, the loading platen was attached to the hydraulic piston through the load cell 1# (HBM U2A tension/compression load cell with a measurement range of 0–50 kN and accuracy of ±5 N), used to measure the compressive force applied by the piston. Thus, the load measure by cell 1# corresponds to F_p in Fig. 2. On the rear side, back-platens 1# and 2# were attached to the frame through load cells 2# and 3# and, 4# and 5#, respectively (load cells 2#-5# were VETEK 101BH S-beam load cells with a range of 0–50 kN and accuracy of ±8.5 N). Therefore, the setup allowed independent measurement of forces transmitted through each of the two contacts corresponding to loads F_1 and F_2 in Fig. 2. The displacement gauge, LVDT 1# (Linear Variable Differential Transducer of HBM WA-L with range 0–500 mm and accuracy of ±0.1 mm) was attached to the frame and measured the movements of the loading platen with respect to the frame. All load cells, LVDT and EHSV, were connected to a data acquisition processor (DAP; Data Translation DT9834 with a sampling rate of 1000 Hz). DAP was connected to a computer installed with the data acquisition-control software (TDRec). The experiment setup was controlled by TDRec under a closed-loop force-control system using the force measurement from load cell 1# and EHSV signal.

The procedure of the three-block breakage experiment was as follows. First, the ice blocks were placed in the test basin with the required *c*. Attention was paid to remove slush at the contact interfaces (slush was due to freezing at the surface of the water in the test basin). Subsequently, the piston was moved forward and an initial compressive force of 0.3 kN was applied to the specimens. This initial force resulted in uniform contact between the ice specimens and the loading platen. The reading for LVDT 1# was set to zero after setting the initial force. Then, the test was started from TDRec. During the test, the piston force increased linearly at a rate of 5 kNs^{-1}, until the ice specimens broke. The loading rate was chosen so that creep would not have a significant effect on the ice specimens, while having the experiments long enough to be able to study the progressive failure of the ice blocks.

Table 1
Experiment matrix. In the table, *c* is the contact length, 'contact area' is the total contact area of two contacts (2 × *c* × ice thickness), 'increase rate of nominal contact stress' is the increase rate of stress at contact calculated by dividing the increase rate of total loading force by the contact area.

Experiment type	*c* [mm]	Contact area [$m^2 \times 10^{-2}$]	Increase rate of nominal contact stress [$MPas^{-1}$]	Number of experiments
Three-block breakage experiment	25	0.55	0.91	4
	50	1.10	0.45	4
	75	1.65	0.30	5
	100	2.20	0.23	8
	125	2.75	0.18	5
	150	3.30	0.15	6
Compressive strength experiment	–	–	0.15	6

Table 2
Failure forces and failure plane properties of uniaxial compressive tests. max(F_p) is the maximum piston force, θ represents the angle between failure plane and loading direction, and $A\tau$ is the failure plane area.

Experiment no.	max(F_p) [kN]	θ	A_τ [$m^2 \times 10^{-2}$]	Compressive strength [kPa]
C1	28.4	28°	8.27	859.2
C2	29.0	31°	5.62	879.5
C3	20.7	33°	6.37	627.0
C4	30.4	28°	7.71	921.2
C5	18.5	30°	6.68	559.1
C6	27.5	30°	6.19	834.5

2.3. Test matrix

Thirty-two breakage experiments were conducted using six contact lengths varying from $c = 25$ to 150 mm (Fig. 2). Table 1 presents the experiment matrix. In addition to the breakage experiments, six uniaxial compression experiments were conducted at various stages of the campaign to evaluate the compressive strength of the ice for consistency. The compressive strength experiments employed ice specimens that were grown similarly to other specimens but having nominal dimensions of 600 mm × 300 mm × 110 mm. Table 2 summarizes those results. Uniaxial strength of the ice was calculated by dividing the maximum piston force, max(F_p) by the cross-sectional area of the specimens (300 mm × 110 mm). Ice properties remained relatively constant throughout the campaign: Measured compressive strength of the specimens was on average 780.1 kPa and had a relative standard deviation of about 20%. Compressive strength values obtained here are in agreement with the field measurements presented by Moslet (2007), who reported in situ horizontal compressive strength of 800 kPa (but with a higher relative standard deviation of about 40% as calculated from the reported data) for saline ice samples taken through the whole thickness of the sea ice sheet having temperature of −1 °C.

3. Results

3.1. Piston force and contact force records

Fig. 4 presents typical piston force-time, F_p-*t*, and piston force-displacement, F_p-*d*, curves from the experiments with contact lengths $c = 50$, 75 and 125 mm. As shown in the figure, F_p-records were distinctly nonlinear for small contact lengths, *c*. However, for large

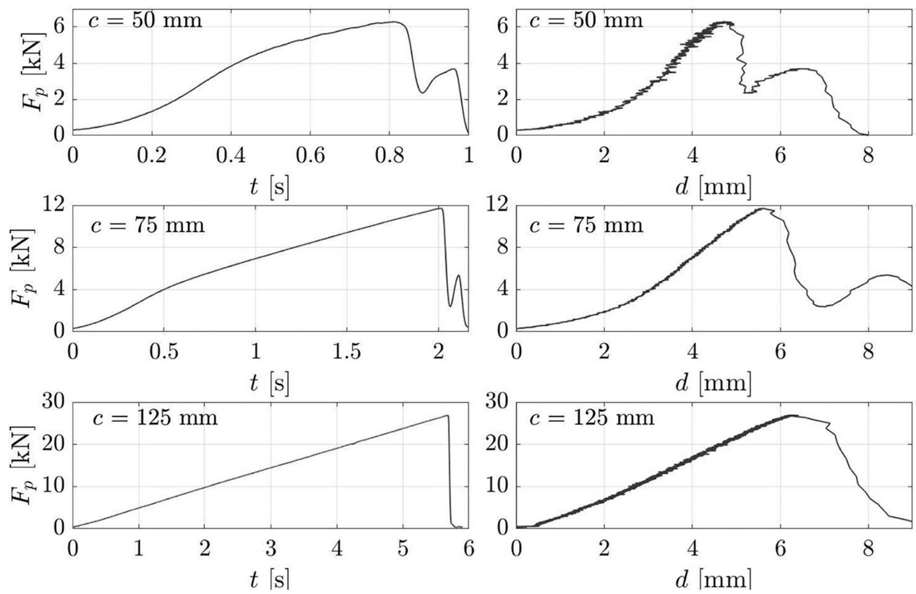

Fig. 4. Typical piston force, Fp, records from three experiments with contact lengths, *c* as indicated: left column shows *Fp* plotted against time, *t*, and right column against piston displacement *d*.

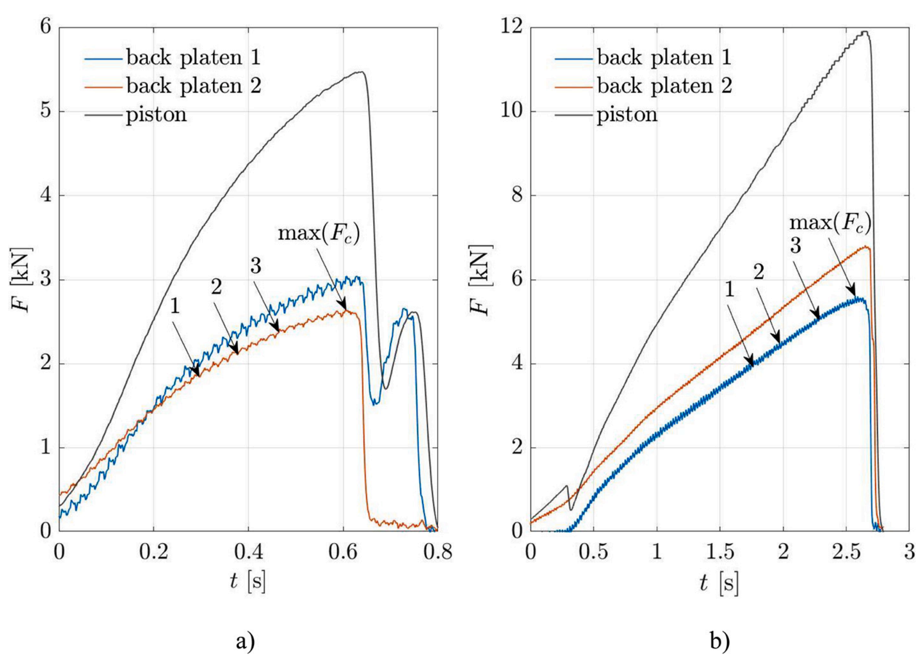

Fig. 5. Typical *F*-*t* curves for contact lengths (a) $c = 50$ mm and (b) $c = 100$ mm. Markers 1–3 in the figures indicate time instances with 70%, 80% and 90% of maximum contact force, max(F_c), respectively. Figs. 7 and 8 show snapshots of the two experiments from time instances 1–3 and max(F_c).

contact lengths, F_p-records had a significant linear portion with nonlinear parts at the start and near the peak. The nonlinear behavior at the start of each test was partly due to the system of three blocks settling at its contacts. The nonlinearity close to the peak was due to the formation of microcracks and local inelastic deformation on the failure planes; thus, the failure could be characterized as quasi-brittle. The F_p-levels increased with c. Failure within the system of three blocks could be identified by the sudden drop in the F_p -curves. The failure occurred within few seconds from the start of the test with the piston displacement of about 5 mm; overall stiffness of the block array with $c = 50$ mm was about a quarter of that of with $c = 125$ mm.

Fig. 5a and b present F_p-records from two experiments, which respectively had $c = 50$ and 100 mm. In addition to F_p-records, the figures show the reaction forces F_1 and F_2 (Fig. 2), which were the contact forces transmitted by the two block-to-block contacts, from the same two experiments. As the figures demonstrate, the difference between the two contact forces during the period of increasing load was typically less than 10%; the difference between the sum of the contact forces and F_p was on average less than 5%. Both F_1 and F_2 curves followed a similar trend as the F_p curve. These features demonstrate that the experimental set-up behaved well, that the contacts were well-settled and that the loading was close to symmetrical. It was typical that the failure first occurred at one of the contacts, immediately after which, the failure at the second contact took place, since the total piston load, F_p became transmitted by it. The maximum contact force, max(F_c), was defined as the contact force leading to the first failure. The second

Table 3
Failure forces and failure plane properties. c is the contact length. "Ice sheet number" is the identification number of ice sheet where ice blocks were harvested from, max(F_p) is the maximum piston force and max(F_c) represents the maximum contact forces of the first contact to fail. Column "1st failure" indicates, which contact (according to Fig. 2) failed first, and 'Failure mode' indicates the mode of failure of the first contact. Further, θ is the angle between failure plane and loading direction; and $A\tau$ represents the failure plane area.

Experiment no.	c [mm]	Ice sheet no.	max(F_p) [kN]	max(F_c) [kN]	1st failure	Failure mode	θ	A_τ [$m^2 \times 10^{-2}$]
B1	25	1	1.5	1.0	2	Crushing	26°	0.51
B2	25	2	4.3	2.4	2	Shear	25°	0.63
B3	25	7	3.2	1.8	2	Shear	30°	0.67
B4	25	13	4.2	2.6	1	Crushing	24°	0.65
B5	50	1	5.5	2.6	2	Shear	33°	1.05
B6	50	2	7.3	3.8	2	Crushing	24°	0.97
B7	50	6	6.3	3.2	2	Shear	24°	1.21
B8	50	13	6.6	3.0	1	Shear	19°	1.63
B9	75	1	9.1	5.1	2	Shear	28°	1.97
B10	75	6	8.5	5.1	2	Splitting	0°	3.37
B11	75	6	12.5	6.9	2	Shear	21°	1.95
B12	75	7	11.7	5.7	1	Shear	21°	1.97
B13	75	11	19.0	10.4	2	Shear	29°	1.63
B14	100	1	11.9	5.6	1	Shear	25°	2.01
B15	100	2	16.2	8.7	2	Shear	15°	3.44
B16	100	3	13.4	7.0	1	Shear	18°	3.49
B17	100	3	21.2	11.2	2	Shear	22°	3.54
B18	100	3	20.3	9.3	1	Y-shaped	–	–
B19	100	5	11.1	5.9	2	Splitting	5°	3.37
B20	100	10	16.3	8.2	1	Splitting	10°	3.55
B21	100	12	18.2	9.5	2	Shear	14°	3.44
B22	125	4	16.0	7.6	2	Y-shaped	–	–
B23	125	4	16.6	8.8	1	shear	16°	3.51
B24	125	5	21.2	10.8	2	Shear	22°	3.62
B25	125	7	13.8	6.1	1	Shear	15°	3.47
B26	125	7	20.9	9.4	2	Shear	23°	3.54
B27	150	5	26.5	11.8	1	Shear	27°	3.72
B28	150	8	25.4	13.2	1	Shear	26°	3.70
B29	150	9	23.9	12.5	1	Shear	20°	3.74
B30	150	9	18.0	9.1	1	Shear	22°	3.64
B31	150	11	19.2	8.9	2	Splitting and shear[a]	19°	3.49
B32	150	11	33.6	17.0	1	Splitting and shear[a]	19°	3.66

[a] Splitting failure in tests B31 and B32 are intermediate state and F_p kept increasing after the failure. Fig. 9f shows the failure patterns for these cases, and discussed further in Section 3.3.

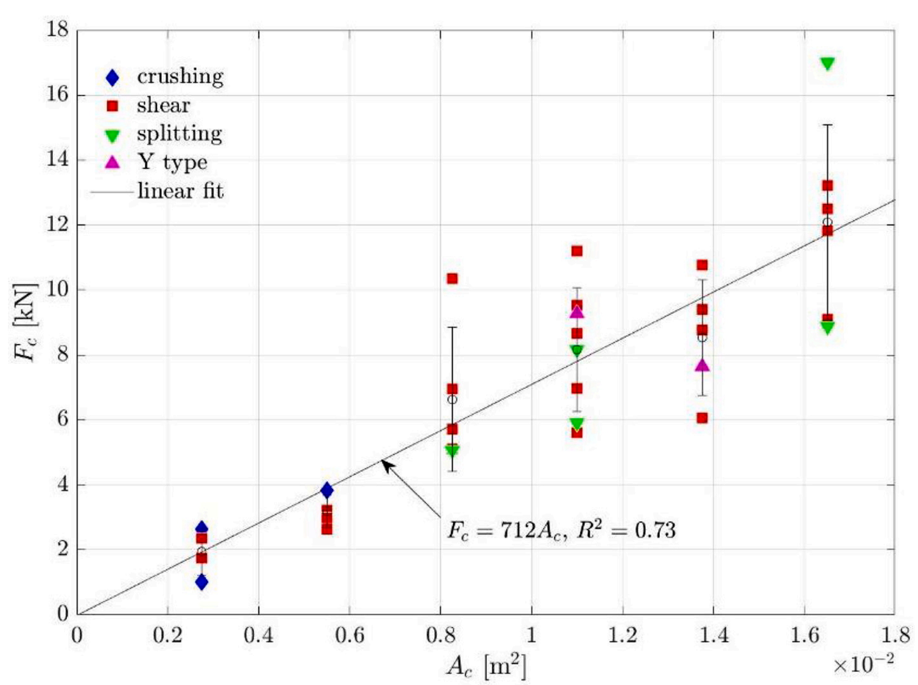

Fig. 6. Maximum contact force, max(F_c), plotted against contact area, A_c. Marker type indicates the failure mode given in the legend. The best-fit line was not forced to pass through the origin.

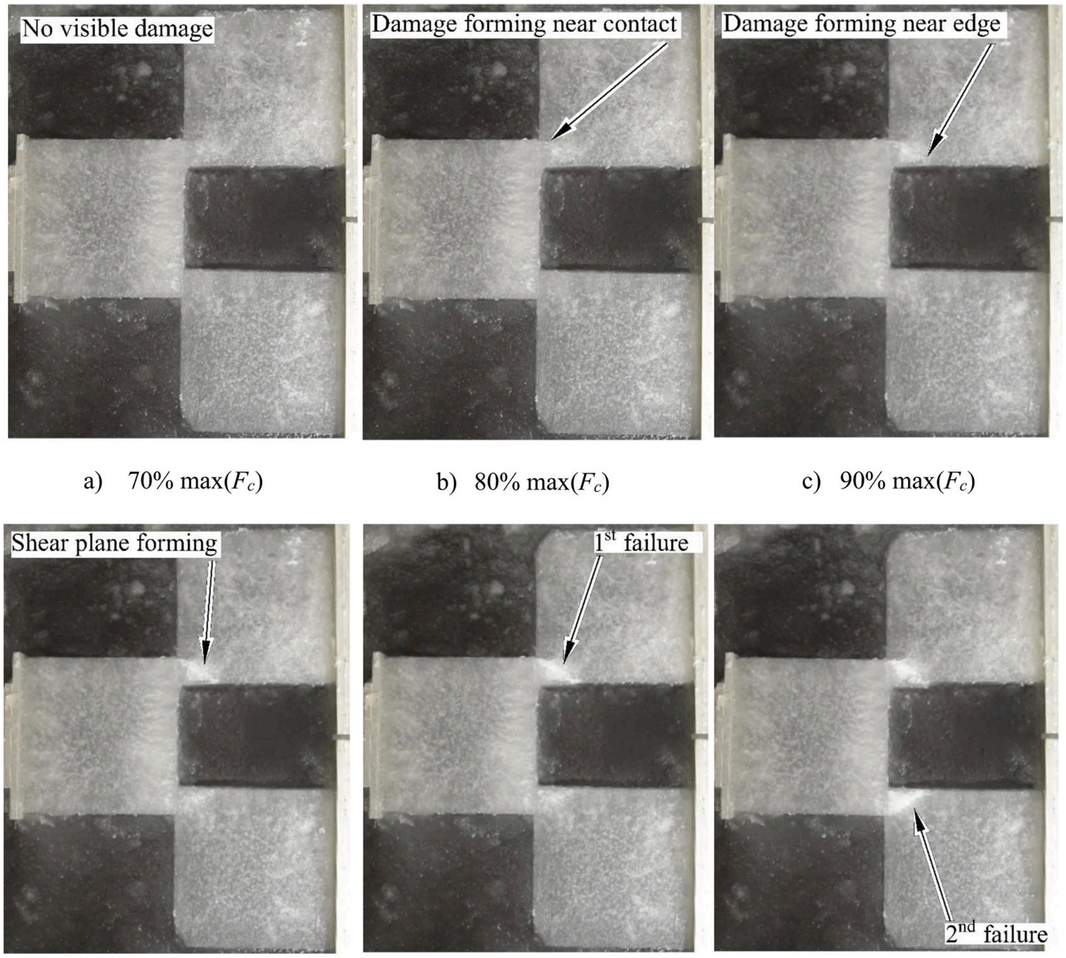

d) max(F_c) e) Instance of first failure f) Instance of second failure

Fig. 7. Failure process of the c = 50 mm experiment.

contact failed immediately after the first with a load having magnitude within 80–120% of max(F_c). Since max(F_p) and max(F_c) were often measured well after the F_p-d curve had become linear, it is reasonable to assume that initial settling at the contacts did not have any significant influence on their values. Further, it is important to notice that max(F_c) was reached slightly before the load drop, indicating the actual failure. Table 3 summarizes the results from all the experiments.

Fig. 6 reports the values of max(F_c) plotted against the nominal contact area, A_c, simply defined as the product of the contact length and ice thickness. In addition, the figure shows a trend line fitted to the data. Even if the values of max(F_c) are somewhat scattered, they show an expected increasing trend with the area of contact, and hence with the contact length; relative standard deviation for max(F_c) is about 25%, close to the value obtained in the uniaxial compression experiments, giving further confidence on trends seen in the data. The slope of the trend line of Fig. 6 suggests that the critical nominal compressive contact stress has a value of 712 kPa. As will be discussed below, however, the values of max(F_c) were not limited by the compressive failure of ice.

3.2. Failure process

Figs. 7 and 8 present six-photo sequences from the two experiments with the load records in Fig. 5a and b, respectively. The first four photos of each sequence are from the four time instances, 1–3 and max(F_c), indicated in Fig. 5a and b. The final two photos of each sequence are from the instances of the first and the second failure, respectively. The mode of the first failure in both cases shown was shear. Further, the figures indicate that the second failure in the experiment with c = 50 mm was also due to shear (Fig. 7f), but in the experiment with c = 100 mm, the second failure showed Y-shaped failure patterns (Fig. 8f).

Figs. 7 and 8 importantly show the material damage appearing as bright white bands on the areas of the final failure planes before the instance of the failure. This visual effect was the result of microstructural damage accumulating along the eventual failure plane. The width of these bands was 7–9 mm, which is about three times the grain size. Material softening due to microcracks was one of the reasons for the nonlinearity close to the peak in the force records presented in Figs. 4 and 5. Overall, the failure process of the ice blocks can be considered as quasi-brittle. In more detail, Fig. 7b first shows microcracking in the areas near the contact edge. As the force increased further, more microcracks started to grow near the areas of the edge of the ice blocks (Fig. 7c). Post-experiment inspection also showed some damage at the block corners, likely increasing during the test with the load. When the contact force had almost reached max(F_c), a thick white line indicating the location of the macroscopic failure plane, consisting of a dense network of interconnected smaller microcracks, was forming (Fig. 7d). Similar bands of material, showing incremental damage before the failure, were observed in all experiments. Finally, as the contact force passed max(F_c), the macroscopic shear-like failure occurred along the shear plane (Fig. 7e). Subsequent second failure revealed a similar failure process. The formation of the second failure was faster and typically started immediately towards the end of the first failure

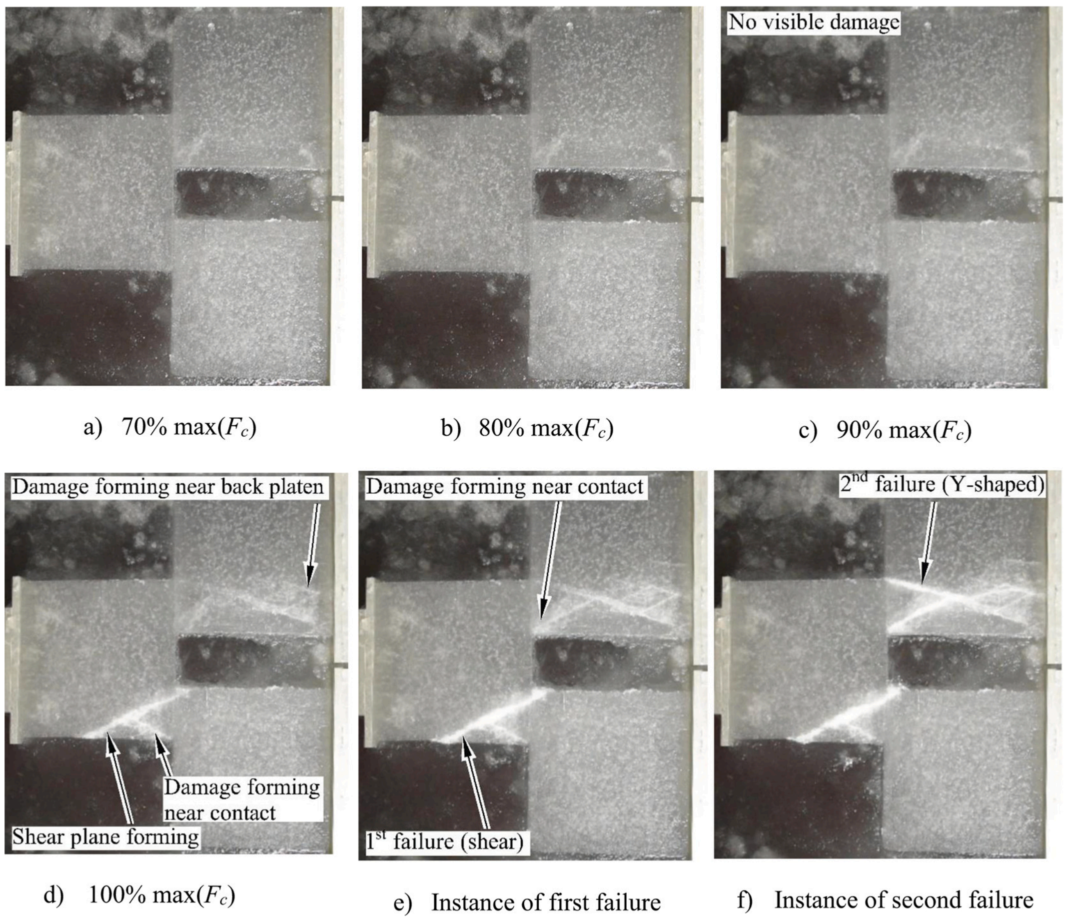

Fig. 8. Failure process of the c = 100 mm experiment.

(Fig. 7f). The process described above was observed consistently in all of the experiments and, as discussed below, the value of max(F_c) was dependent on the length of the shear bands. It should be mentioned that many ice failure problems can be explained based on fracture mechanics analysis, but the failure process in the experiments here show no evidence of crack propagation. Rather, the failure planes became evident as microstructural damage accumulated along them. Further, there was no evidence that these failure planes deviated appreciably from a straight path (see Figs. 8d,e,f and 9), as would be expected if the failure was governed by crack propagation (Thouless et al., 1987; Kujala, 1994). Thus, the failure process observed in these experiments was due to the strength of the material rather than sudden crack propagation caused by stress concentrations at the contact.

The failure process presented in Fig. 8 shows similar behavior as described in Fig. 7. Microcracks first started to form near contacts and edges, followed by the formation of macroscopic shear plane. However, the process was faster and appeared at a later stage of loading (Fig. 8d). It is important to notice that a second macroscopic damage zone initiated from the contact as seen in Fig. 8d. This feature, however, did not evolve into a failure plane and the contact failed by shearing. The final three photos of Fig. 8, additionally, show a Y-shaped failure occurring at the second contact. In this type of failure, microcracking typically initiated from the areas near the back-platens. Microcracks formed in pairs, which had an approximate 45° angle between them. As the contact force increased, microcracks also started to form near the corners of the contact, similar to shear-like failures. Finally, two macroscopic failure planes formed as the microcracks initiated from the back-platen reached the shear-like failures.

3.3. Failure patterns

Fig. 9 summarizes failure patterns for all c on a more general level. The failure planes in the figure were sketched based on the photos from the experiments. As Fig. 9 suggests and Table 3 summarizes, the dominant failure mode was shear as it occurred in 75% of the experiments. In some cases with c = 25 mm, the blocks failed by crushing and with c = 150 mm, by splitting. Occasionally, a Y-shaped failure, seen in Fig. 8f, was also observed in some experiments with $c \geq 100$ mm. Results shown in Fig. 6 indicate that, on average, there were no systematic or significant variations in max(F_c) as a function of failure mode.

Note that when splitting did occur, in the experiments with c = 150 mm, the contact still transmitted force. Fig. 9f illustrates how splitting (marked with red) created an ice column that carried the contact load until the shear failure occurred (marked with blue). A slight force drop could be seen at the instance of splitting, but the force kept on increasing after the drop. Maximum contact force at the instance of the subsequent shear failure was considered as max(F_c) in these cases. On the other hand, with c = 25 mm, highly damaged zones formed throughout the contact length, leading to crushed material close to the contact interface. When c = 150 mm, the two blocks (which are not in contact in any of the other tests), were touching each other. Even if this contact could be assumed to lead to some confinement on them, the dominant failure mode was still the above-described shear-like failure. Thus, the effect of this confinement was negligible.

3.4. Contact behavior

Interestingly, contact settling occasionally led to freezing at the contact interface. Fig. 10 presents a horizontal thin section of a frozen

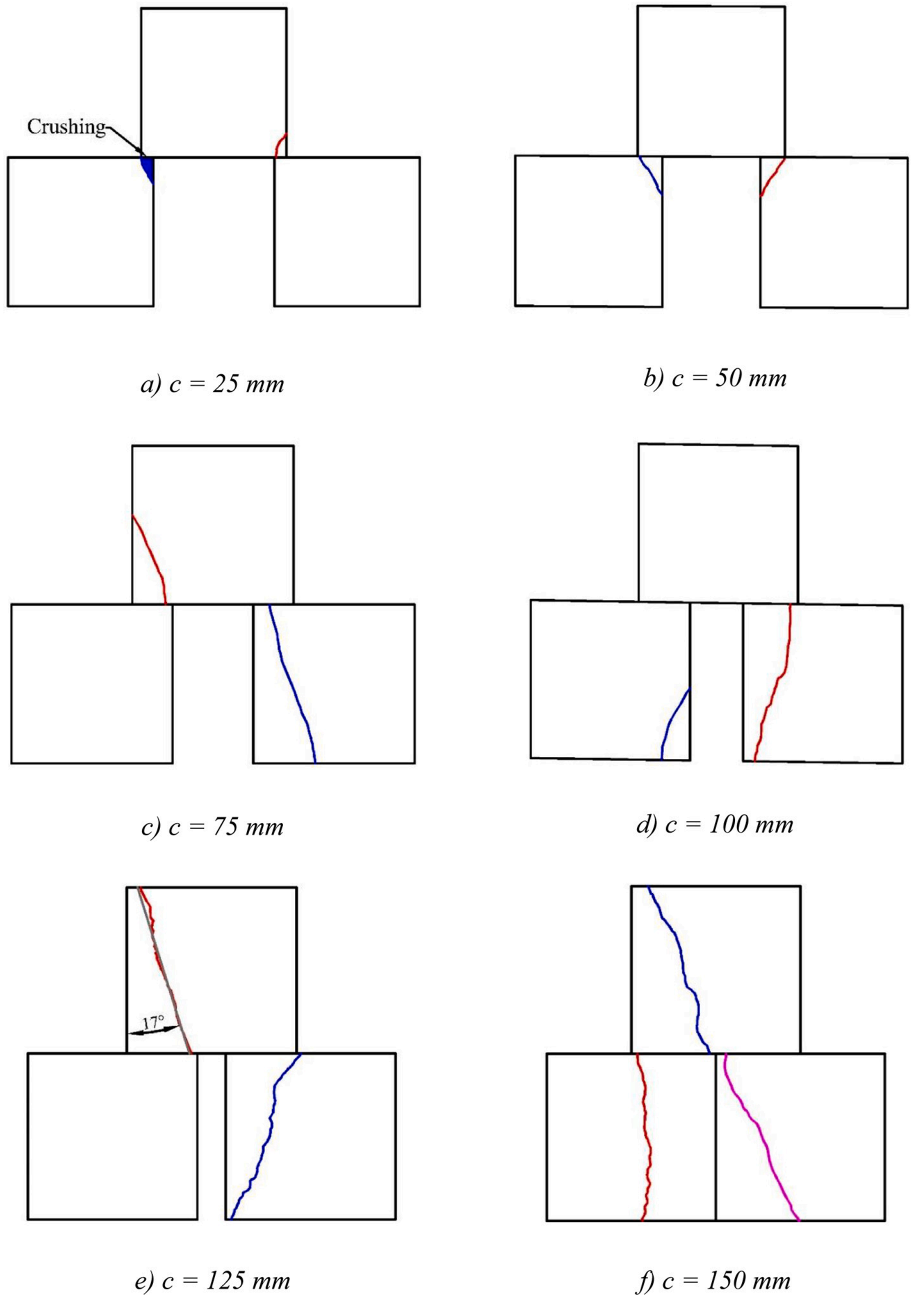

Fig. 9. Representative failure patterns for all contact lengths: (a) $c = 25$ mm, (b) $c = 50$ mm, (c) $c = 75$ mm, (d) $c = 100$ mm, (e) $c = 125$ mm and (f) $c = 150$ mm. First failure is shown with red, second with blue and third with purple lines. Failure angle was described as shown in (e).

contact. The figure shows that the contact interface has a uniform layer of very fine ice crystals, likely resulting from freezing after contact. Further, there are no visible gaps in the contact interface. Thus, it seems that some combination of localized deformation, freezing and perhaps recrystallization at the contact interface created a uniform contact between the ice blocks. To check whether this freezing was related to the initial holding time (the period of having the blocks pressed together with initial low pressure), we performed nine additional tests with initial holding times of 15, 30 and 45 min. The results showed no apparent correlation between initial holding time and the occurrence of freezing at the contact; there was no change in the maximum load values nor in the block failure modes for the range of holding times examined.

4. Analysis and discussion

4.1. Shear failure in contact

The results presented above make it clear that floating ice blocks under ice-to-ice contact forces fail primarily due to the development of shear faults. Signs of such failure mode are apparent from Figs. 7 and 8, which show failure planes resembling Coulombic shear faults, a common failure mechanism of ice under low axial confinement (Golding et al., 2010). Coulombic failures were often characterized by failure planes formed of interconnected microcracks and 20° to 30° angle with respect to the principal stress direction. Moreover, the Y-shaped failure seen in Fig. 8f can be regarded as a 'conjugate Coulombic failure', a variation of Coulombic faults (Golding et al., 2010).

For shear-like failures, the critical shear force resolved on the failure

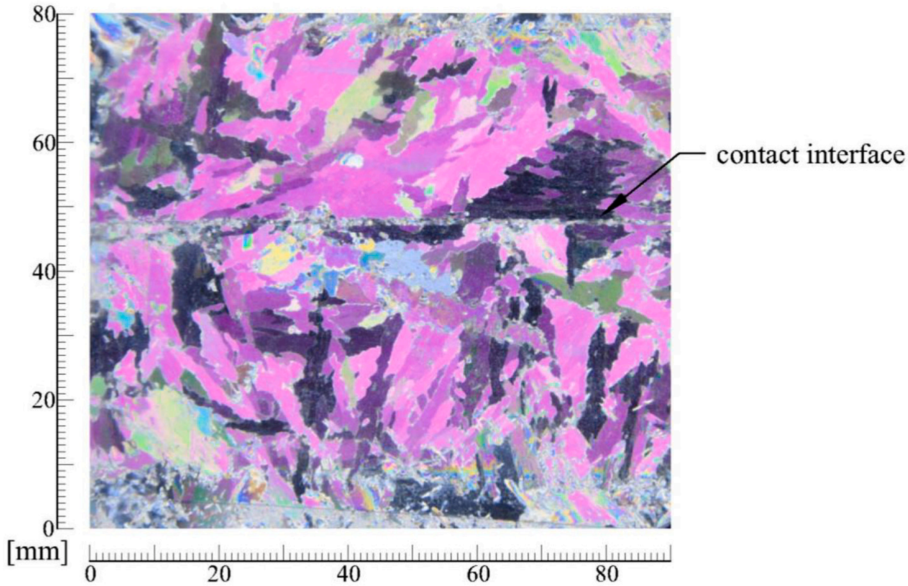

Fig. 10. Thin section results of a frozen contact.

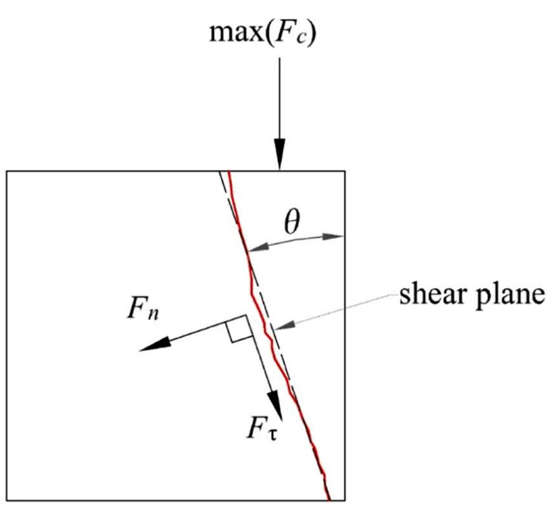

Fig. 11. Normal and shear forces resolved on the failure plane for quasi-static force equilibrium at critical moment of shear failure. max(*Fc*) is the maximum contact force. *Fτ* and *Fn* are shear and normal forces along the failure plane respectively. θ is the failure angle.

plane was calculated as indicated in the Fig. 11. At the instance of max (F_c), the requirement for force equilibrium yields equations,

$$F_n = max(F_c) \cdot sin(\theta) \tag{1}$$

$$F_\tau = max(F_c) \cdot cos(\theta) \tag{2}$$

where, F_τ and F_n are the critical shear and normal force resultants aligning with and perpendicular to the shear plane having an angle θ, respectively. For calculating F_τ, the value for max(F_c) is directly available from the experiments and θ can be obtained by fitting a straight line along the failure plane (Fig. 9e). The line fitting was done by first tracing the failure plane using the images from the experiments, and then by using MATLAB for fitting a line through the data points formed by the traced failure plane. The point density was about 0.2 points per mm in traced failure patterns. By using the fit, the length of the failure plane was estimated with reasonable accuracy and the area of failure plane, A_τ, was calculated.

Fig. 12 reports the calculated F_τ values plotted against A_τ for shear-like failures. In addition to the data points, the figure shows a linear fit for the data. The relatively high value of the coefficient of determination, $R^2 = 0.73$, indicates that the linear fit describes the data well and has a physically-sound zero intercept. (Leaving out the two offset data points, from the two specimens originating from the same ice sheet, would yield an approximately equal linear fit having $R^2 = 0.90$). The slope of the fit, 279 kPa, represents the shear strength of ice. Therefore, the maximum contact force was limited by the shear strength of the ice. This notion simplifies the contact force models for ice. The shear strength obtained here is lower than the 560 kPa reported for isothermal, drained, columnar sea ice at −2 °C (Frederking and Timco, 1986). The lower shear strength in the present effort is likely due to the relatively warm specimens and their naturally occurring temperature gradient. We could not, however, explore this point further by testing dry, isothermal, specimens since they would have led to peak loads too high for the experiments to be performed safely using our setup. Moreover, Timco and Weeks (2010) emphasized that the results of shear strength measurement depend on the loading conditions, which may lead to normal stresses acting on the failure plane. When the ice blocks are loaded as in the experiments here, this is likely the case.

4.2. Comparison of failure in contact: Ice-to-ice vs. ice-to-metal

Results of this study suggest that contacting ice blocks under compression are likely to experience shear-like failure. This observation stands in contrast to observations of failure due to crushing and flaking at the ice block edge (Fransson et al., 1991; Tuhkuri, 1995) for the case of an ice-metal interface. These previous experiments primarily involved wedge-shaped, isothermal, confined ice specimens pushed against a rigid metal platen. Fransson et al. (1991) describe the ice failure process at contact as continuous crushing, beginning with flaking and followed by breaking off of larger ice pieces due to propagating cracks. Moreover, they argued that wedge-shaped specimens yielded stable and continuous crushing at the contacts. Tuhkuri (1995) reported that the confinement on the ice blocks prevents the formation of splitting or shear-failure in wedge-shaped specimens, increasing the possibility of crushing failure at the contact. Määttänen et al. (2011) also observed similar local crushing behavior with an initially flat contacting face.

In the above experiments with an ice-metal interface, failure involved crushing with the development of high-pressure zones (Riska,

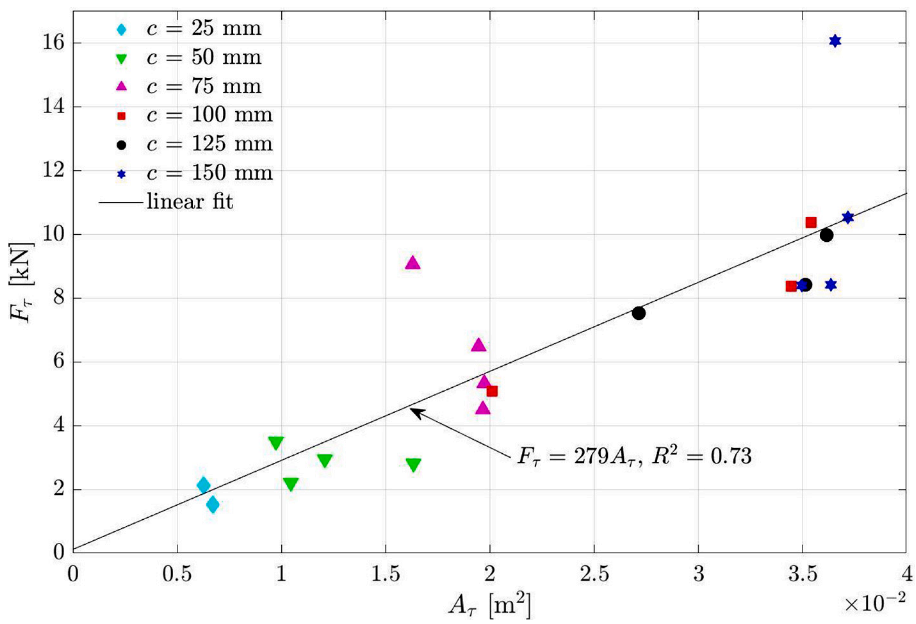

Fig. 12. Critical shear force $F\tau$ vs. failure plane area $A\tau$.

1991). Stress concentrations at these high-pressure zones may generate microcracks, leading to local failure at the contacting facet of the specimen. Therefore, it seems that the crushing observed in ice-metal experiments is due to a combined effect of shape of the contacting facet, confinement of the ice block and the line-like contact developing in the ice-metal interface during the continuous crushing of the specimen. Additionally, the confinement around the high-pressure zones may be affected by the overall shape and size of the specimens (Palmer et al., 2009). Moreover, Kuehn et al. (1993) argue that high-pressure zones in ice-metal contacts are due to perturbations in the ice contact surfaces, which may flatten out when ice is deformed sufficiently slowly, thus reducing the stress concentrations at the contact. In contrast, the contact surfaces of the floating ice blocks used in the present study were wet and close to their melting temperature. Furthermore, accurate control over the specimen geometry and surface finishing by the molds could have also minimized the perturbations. Hence, it is possible that the local inelastic deformation, either viscoelastic or plastic, at the contact could flatten out the perturbations and surface asperities without causing significant microcracking. The thin section presented in Fig. 10 appears to confirm this hypothesis. In addition to the shear band and eventual failure along it (Figs. 7 and 8), we observed no signs of distinct cracks propagating from the contact interface, which is contrary to the above-described crushing process of ice in ice-metal contact. It is thus unlikely that local failure at the contact interface played a significant role in the present experiments, allowing the contacts to transmit the force required to break the ice block by shearing.

The present results have implications on numerical modeling of ice-structure interaction processes. As mentioned above, Discrete Element and Combined Finite-Discrete Element Method simulations, have become popular tools in ice mechanics (Tuhkuri and Polojärvi, 2018). In such simulations, simplified contact force models are typically used and it has been common to choose the upper limit for the maximum contact force based on the contact area and the compressive or crushing strength of ice (Hopkins, 1992; Paavilainen et al., 2009; Paavilainen and Tuhkuri, 2013; Ranta and Polojärvi, 2019; van den Berg et al., 2018). That approach assumes that the contact force is limited by the local crushing failure at the ice-to-ice contacts (Ranta and Polojärvi, 2019). The results here indicate that this choice for the upper limit may often not be correct when simulating ice behavior, but the shear-like failure of ice blocks must be also considered. For example, the maximum loads in the simulations by Ranta and Polojärvi (2019) could have roughly been only about 75% of those observed had the shear-like failure been taken into account. It is important to notice that the choice of the load-limiting parameter will depend on the assumed mode of ice failure.

5. Conclusions

Laboratory experiments on ice block breakage involving ice-to-ice contacts were conducted using a recently developed apparatus designed to apply in-plane compressive loads to floating specimens. The test material was laboratory-grown saline ice with an unaligned columnar microstructure. The aim was to gain insight into the mechanism of ice block breakage as it applies to force transmission in ice rubble fields. It is believed that force transmission in ice rubble is limited by the stability of force chains within the rubble and this stability is, in turn, limited by either buckling or failure at the ice-to-ice contacts. The present effort focused on quantifying the latter mechanism and established that the predominant mechanism of failure at ice-to-ice contacts of floating blocks is shear faulting. For specimens with an average temperature of -2.5 °C and subjected to a loading rate of 5kN s^{-1} following conclusions may be drawn.

1. The primary mode of failure for the ice blocks in contact and under compression was shear. This should be accounted for in numerical modeling and in ice load models related to force chains (Section 4.2).
2. Failure planes observed in the experiments had the characteristics of 'Coulombic shear faults'. Occasionally other failure modes, such as crushing and 'Y-shaped' failure planes were detected. The latter appeared to be due to 'Coulombic shear faulting' as well (Section 3.2 and Figs. 7 and 8).
3. Maximum ice-to-ice contact force an ice block can withstand had a linear relationship with contact area and was limited by the shear strength of the ice. For the ice specimens used in this study, shear strength was found to be 279 kPa (Section 4.1 and Figs. 6 and 12).
4. Ice-to-ice contacts deformed locally and adjusted themselves under low compressive stresses. Local deformations at the contact caused nonlinear mechanical behavior in the tested three-block system under low stress conditions (Section 3.4 and Fig. 10).
5. The experimental apparatus used and the procedures followed in this study provided an effective method to study the failure of saline,

floating ice blocks under ice-to-ice contact compressive forces (Section 3.1).

The presented study concentrated on very simple contact geometries and ice block shapes to minimize the variables affecting the results, but additional contact geometries should be used in future studies. In addition, a range of ice types and loading directions related to the crystal structure should be examined.

Author statement

AP and DMC designed the study. MP and MW performed the experiments. All authors contributed to the interpretation of the results. MP drafted the paper. All authors commented on the text.

Declaration of Competing Interest

The authors declare that they have no known competing financial interests or personal relationships that could have appeared to influence the work reported in this paper.

Acknowledgements

The authors are grateful for the financial support from the Academy of Finland through the project (309830) Ice Block Breakage: Experiments and Simulations (ICEBES). AP worked on the article while visiting Thayer School of Engineering at Dartmouth College (Hanover, NH, USA) during spring 2020. Thanks are extended to Prof. Erland Schulson for hosting and for valuable discussions on the topic of this paper. Finnish Maritime Foundation is acknowledged for partial funding of the visit.

References

Chang, X., Lu, J., Wang, S., Wang, S., 2018. Mechanical performances of rock-concrete bi-material disks under diametrical compression. Int. J. Rock Mech. Min. Sci. 104, 71–77. https://doi.org/10.1016/j.ijrmms.2018.02.008.

Cleary, P., 2001. Modelling comminution devices using DEM. Int. J. Numer. Anal. Methods Geomech. 25, 83–105. https://doi.org/10.1002/1096-9853(200101)25:1<83::AID-NAG120>3.0.CO;2-K.

Cole, D.M., Dempsey, J.P., 2004. In situ sea ice experiments in McMurdo Sound: Cyclic loading, fracture, and acoustic emissions. J. Cold Reg. Eng. 18, 155–174.

Daley, C., Tuhkuri, J., Riska, K., 1998. The role of discrete failures in local ice loads. Cold Reg. Sci. Technol. 27, 197–211. https://doi.org/10.1016/S0165-232X(98)00007-X.

Daouadji, A., Hicher, P.-Y., 2010. An enhanced constitutive model for crushable granular materials. Int. J. Numer. Anal. Methods Geomech. 34, 555–580. https://doi.org/10.1002/nag.815.

Delaney, G.W., Morrison, R.D., Sinnott, M.D., Cummins, S., Cleary, P.W., 2015. DEM modelling of non-spherical particle breakage and flow in an industrial scale cone crusher. Miner. Eng. 74, 112–122. https://doi.org/10.1016/j.mineng.2015.01.013.

Einav, I., 2007. Breakage mechanics-part I: Theory. J. Mech. Physics Solids 55, 1274–1297. https://doi.org/10.1016/j.jmps.2006.11.003.

Fransson, L., Olofsson, T., Sandkvist, J., 1991. Observations of the failure process in ice blocks crushed by a flat indentor. In: Proceedings - International Conference on Port and Ocean Engineering under Arctic Conditions. POAC, pp. 501–514.

Frederking, R., Timco, G.W., 1986. Field measurements of the shear strength of columnar-grained sea ice. In: Proceedings - 8th International Association for Hydraulic Research Symposium on Ice, vol. I, pp. 279–292.

Gagnon, R.E., 2018. New insights about ice friction obtained from crushing-friction tests on smooth and high-roughness surfaces. Int. J. Naval Archit. and Ocean Eng. 10, 361–366. https://doi.org/10.1016/j.ijnaoe.2018.02.002.

Golding, N., Schulson, E.M., Renshaw, C.E., 2010. Shear faulting and localized heating in ice: the influence of confinement. Acta Mater. 58, 5043–5056. https://doi.org/10.1016/j.actamat.2010.05.040.

Hopkins, M.A., 1992. Numerical simulation of systems of multitudinous polygonal blocks. In: Technical Report 92–22. CRREL, Cold Regions Research and Engineering Laboratory, 69 pp.

Ji, S., Di, S., Liu, S., 2015. Analysis of ice load on conical structure with discrete element method. Eng. Comput. (Swansea, Wales) 32, 1121–1134. https://doi.org/10.1108/EC-04-2014-0090.

Ji, S., Di, S., Long, X., 2017. DEM simulation of uniaxial compressive and flexural strength of sea ice: Parametric study. J. Eng. Mech. 143 https://doi.org/10.1061/(ASCE)EM.1943-7889.0000996.

Kolari, K., 2017. A complete three-dimensional continuum model of wing-crack growth in granular brittle solids. Int. J. Solids Struct. 115–116, 27–42. https://doi.org/10.1016/j.ijsolstr.2017.02.012.

Kuehn, G.A., Schulson, E.M., Jones, D.E., Zhang, J., 1993. The compressive strength of ice cubes of different sizes. J. Offshore Mech. Arctic Eng. 115, 142–148. https://doi.org/10.1115/1.2920104.

Kujala, P., 1994. Modelling of the ice-edge failure process with curved failure surfaces. Ann. Glaciol. 19, 158–164. https://doi.org/10.1017/s0260305500011150.

Kulyakhtin, S., 2019. Application of continuum breakage mechanics to ice rubble modelling. Cold Reg. Sci. Technol. 165 https://doi.org/10.1016/j.coldregions.2019.102797.

Kuutti, J., Kolari, K., Marjavaara, P., 2013. Simulation of ice crushing experiments with cohesive surface methodology. Cold Reg. Sci. Technol. 92, 17–28. https://doi.org/10.1016/j.coldregions.2013.03.008.

Langway Jr., C.C., 1958. Ice Fabrics and the Universal Stage. U.S. Army Snow Ice and Permafrost Research Establishment.

Määttänen, M., Marjavaara, P., Saarinen, S., Laakso, M., 2011. Ice crushing tests with variable structural flexibility. Cold Reg. Sci. Technol. 67, 120–128. https://doi.org/10.1016/j.coldregions.2011.03.004.

Moore, P.F., Jordaan, I.J., Taylor, R.S., 2013. Explicit finite element analysis of compressive ice failure using damage mechanics. In: Proceedings of the International Conference on Port and Ocean Engineering under Arctic Conditions. POAC.

Moslet, P.O., 2007. Field testing of uniaxial compression strength of columnar sea ice. Cold Reg. Sci. Technol. 48, 1–14. https://doi.org/10.1016/j.coldregions.2006.08.025.

Paavilainen, J., Tuhkuri, J., 2013. Pressure distributions and force chains during simulated ice rubbling against sloped structures. Cold Reg. Sci. Technol. 85, 157–174. https://doi.org/10.1016/j.coldregions.2012.09.005.

Paavilainen, J., Tuhkuri, J., Polojärvi, A., 2009. 2D combined finite-discrete element method to model multi-fracture of beam structures. Eng. Comput. (Swansea, Wales) 26, 578–598. https://doi.org/10.1108/02644400910975397.

Palmer, A.C., Dempsey, J.P., Masterson, D.M., 2009. A revised ice pressure-area curve and a fracture mechanics explanation. Cold Reg. Sci. Technol. 56, 73–76. https://doi.org/10.1016/j.coldregions.2008.11.009.

Peters, J.F., Muthuswamy, M., Wibowo, J., Tordesillas, A., 2005. Characterization of force chains in granular material. Phys. Rev. E Stat. Nonlinear Soft Matter Phys. 72 https://doi.org/10.1103/PhysRevE.72.041307.

Pustogvar, A., Polojärvi, A., Høyland, K.V., Bueide, I.M., 2014. Laboratory scale direct shear box experiments on ice rubble: The effect of block to box size ratio. In: Proceedings of the International Conference on Offshore Mechanics and Arctic Engineering - OMAE. https://doi.org/10.1115/OMAE2014-23646.

Ranta, J., Polojärvi, A., 2019. Limit mechanisms for ice loads on inclined structures: Local crushing. Mar. Struct. 67. https://doi.org/10.1016/j.marstruc.2019.102633.

Ranta, J., Polojärvi, A., Tuhkuri, J., 2018. Limit mechanisms for ice loads on inclined structures: Buckling. Cold Reg. Sci. Technol. 147, 34–44. https://doi.org/10.1016/j.coldregions.2017.12.009.

Riska, K., 1991. Observations of the line-like nature of ship-ice contact. In: Proceedings - International Conference on Port and Ocean Engineering under Arctic Conditions. POAC, pp. 785–811.

Schulson, E.M., 2001. Brittle failure of ice. Eng. Fract. Mech. 68, 1839–1887. https://doi.org/10.1016/S0013-7944(01)00037-6.

Schulson, E.M., Duval, P., 2009. Creep and fracture of ice. Creep and Fracture of Ice. https://doi.org/10.1017/CBO9780511581397.

Schulson, E.M., Gies, M.C., Lasonde, G.J., Nixon, W.A., 1989. The effect of the specimen-platen interface on internal cracking and brittle fracture of ice under compression: high-speed photography. J. Glaciol. 35, 378–382. https://doi.org/10.1017/S0022143000009308.

Thouless, M.D., Evans, A.G., Ashby, M.F., Hutchinson, J.W., 1987. The edge cracking and spalling of brittle plates. Acta Metall. 35, 1333–1341. https://doi.org/10.1016/0001-6160(87)90015-0.

Timco, G.W., Weeks, W.F., 2010. A review of the engineering properties of sea ice. Cold Reg. Sci. Technol. 60, 107–129. https://doi.org/10.1016/j.coldregions.2009.10.003.

Tuhkuri, J., 1994. Analysis of ice fragmentation process from measured particle size distributions of crushed ice. Cold Reg. Sci. Technol. 23, 69–82. https://doi.org/10.1016/0165-232X(94)90012-4.

Tuhkuri, J., 1995. Experimental observations of the brittle failure process of ice and ice-structure contact. Cold Reg. Sci. Technol. 23, 265–278. https://doi.org/10.1016/0165-232X(94)00018-S.

Tuhkuri, J., Polojärvi, A., 2018. A review of discrete element simulation of ice-structure interaction. Philos. Trans. R. Soc. A Math. Phys. Eng. Sci. 376 https://doi.org/10.1098/rsta.2017.0335.

van den Berg, M., Lubbad, R., Løset, S., 2018. An implicit time-stepping scheme and an improved contact model for ice-structure interaction simulations. Cold Reg. Sci. Technol. 155, 193–213. https://doi.org/10.1016/j.coldregions.2018.07.001.

Weeks, W., Hibler, W.D., 2010. On Sea Ice. University of Alaska Press, Fairbanks, AK.

Wei, M., Polojärvi, A., Cole, D.M., Prasanna, M., 2020. Strain response and energy dissipation of floating saline ice under cyclic compressive stress. Cryosphere 14, 2849–2867. https://doi.org/10.5194/tc-14-2849-2020.

Zhao, B., Liu, Y., Liu, D., Huang, W., Wang, X., Yu, G., Liu, S., 2020. Research on the influence of contact surface constraint on mechanical properties of rock-concrete composite specimens under compressive loads. Front. Struct. Civ. Eng. 14, 322–330. https://doi.org/10.1007/s11709-019-0594-7.